ACS NANO

www.acsnano.org

ARTICLE

Liquid-Phase Exfoliation of Arsenic Trisulfide (As_2S_3) Nanosheets and Their Use as Anodes in Potassium-Ion Batteries

Harneet Kaur, Bharathi Konkena,[§] Mark McCrystall,[§] Kevin Synnatschke, Cian Gabbett, Jose Munuera, Ross Smith, Yumei Jiang, Raman Bekarevich, Lewys Jones, Valeria Nicolosi, and Jonathan N Coleman*

Cite This: *ACS Nano* 2024, 18, 20213–20225

Read Online

ACCESS | Metrics & More | Article Recommendations | Supporting Information

ABSTRACT: **Here, we demonstrate the production of 2D nanosheets of arsenic disulfide (As_2S_3) via liquid-phase exfoliation of the naturally occurring mineral, orpiment. The resultant nanosheets had mean lateral dimensions and thicknesses of 400 and 10 nm, and had structures indistinguishable from the bulk. The nanosheets were solution mixed with carbon nanotubes and cast into nanocomposite films for use as anodes in potassium-ion batteries. These anodes exhibited outstanding electrochemical performance, demonstrating an impressive discharge capacity of 619 mAh/g at a current density of 50 mA/g. Even after 1000 cycles at 500 mA/g, the anodes retained an impressive 94% of their capacity. Quantitative analysis of the rate performance yielded a capacity at a very low rate of 838 mAh/g, about two-thirds of the theoretical capacity of As_2S_3 (1305 mAh/g). However, this analysis also implied As_2S_3 to have a very small solid-state diffusion coefficient (~10^{-17} m^2/s), somewhat limiting its potential for high-rate applications.**

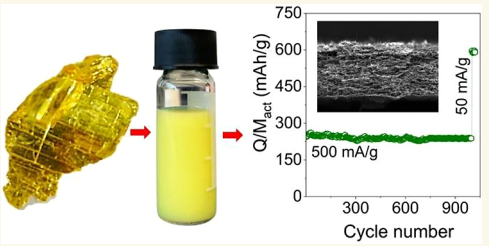

KEYWORDS: *two-dimensional materials, arsenic disulfide, liquid-phase exfoliation, nanosheets, K-ion battery anodes, rate performance*

INTRODUCTION

The escalating global demand for energy storage solutions, driven by the widespread popularity of portable electronic devices,[1] the rise of electric vehicles,[2] and the integration of renewable energy sources,[3] has contributed to the development of lithium-ion batteries (LIBs) as today's predominant energy storage technology.[3,4] However, the relentless expansion of battery usage has highlighted the limited global supply of lithium.[5] In turn, this has raised concerns regarding the vulnerability of our dependence on lithium, prompting a re-evaluation of our energy storage approaches.[5,6] In this context, the spotlight has turned to developing viable alternatives to LIBs. In particular, much attention has been given to batteries based on sodium and potassium ions due to their chemical similarity to lithium.[7−9] Compared to lithium, sodium and potassium are abundant elements and their use in batteries would enhance sustainability and accessibility.[9,10]

While substantial progress has been achieved in the domain of sodium-ion batteries (SIBs),[11,12] the development of potassium-ion batteries (KIBs) is less mature.[8,13,14] There is still a pressing need to develop and characterize new materials for use as both cathodes[15] and anodes[16] in KIBs. For over a decade, the broad family of two-dimensional (2D) layered materials has shown immense promise for use in both LIB and SIB electrodes.[17,18] More recently, these materials have been utilized in the pursuit of new potassium-storing anode materials.[19] The appeal of 2D materials for use in anodes derives from various attributes. For example, the family of 2D materials is very diverse, containing >2000 known materials, each with distinct properties and capabilities.[20] This huge material choice increases the probability of discovering a material with the right combination of properties to meet the specific demands of KIBs. In addition, the ability to convert layered materials into nanosheets via liquid exfoliation[21,22] and subsequently to control their dimensions via size-selection protocols[23] enables a high degree of processability, allowing us to produce electrodes with controlled properties.[24,25] Finally, we might expect diffusion of ions within the interlayer channels in 2D materials to be faster than in 3D materials, leading to better rate performance and enhanced power density.[24−26]

Thus, while 2D materials are very attractive for use in KIBs, only a fraction of the vast array of possible 2D materials has been explored.[19] The quest for high-capacity electrodes had led

Received: March 13, 2024
Revised: July 4, 2024
Accepted: July 9, 2024
Published: July 22, 2024

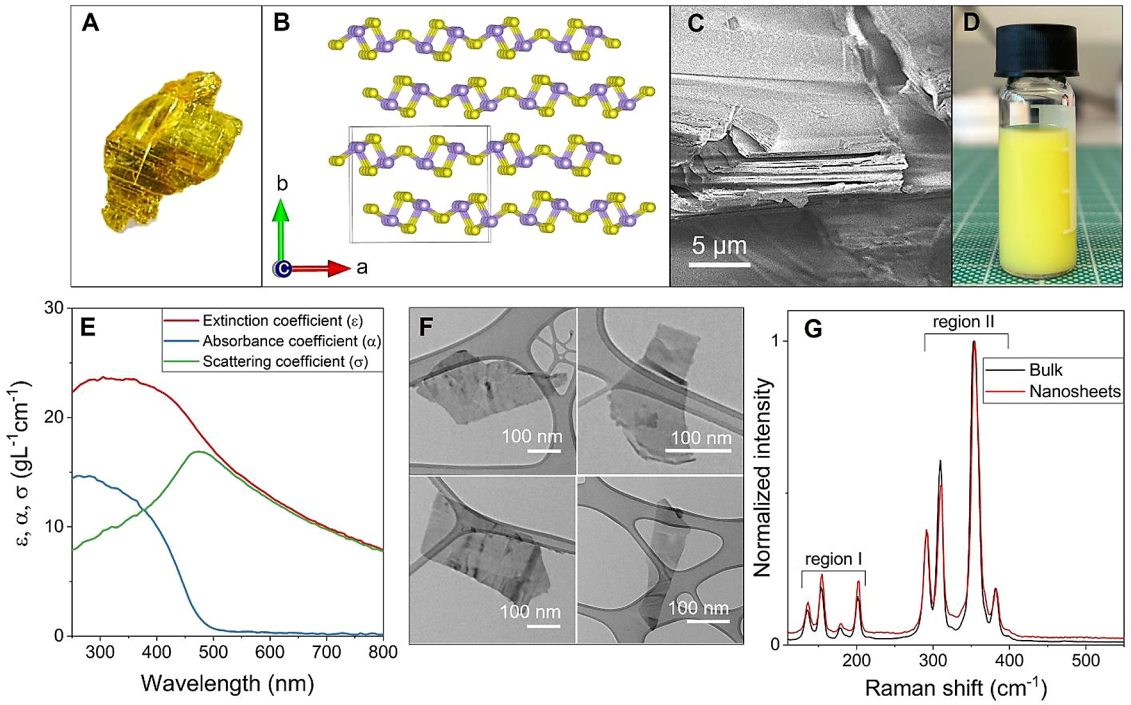

Figure 1. Characterization of liquid-phase exfoliated As_2S_3. (A) Photograph of the mineral orpiment. (B) Crystal structure of bulk As_2S_3, composed of covalently bonded ruffled sheets of As_2S_3 oriented in the (010) direction, held together by weak van der Waals forces. Arsenic and sulfur atoms are depicted as purple and yellow spheres, respectively. The unit cell is represented with a black box and consists of 2 layers with a total of 20 atoms. (C) SEM image of the orpiment crystal surface (as shown in A) displaying multilayered sheets. (D) Dispersed As_2S_3 nanosheets in solvent 2-propanol obtained after liquid-phase exfoliation in an inert atmosphere. (E) Optical extinction, absorbance, and scattering coefficient spectra of the dispersion versus wavelength. (F) TEM images of As_2S_3 nanosheets. (G) Raman spectra comparison between bulk and exfoliated As_2S_3.

to a focus on phosphorus- or sulfur-rich materials such as black phosphorus (b-P, theoretical capacity = 864 mAh/g[27]), tin sulfide (SnS_2, 733 mAh/g[28]), molybdenum disulfide (MoS_2, 670 mAh/g[29,30]), antimony trisulfide (Sb_2S_3, 946 mAh/g[31,32]), or bismuth trisulfide (Bi_2S_3, 625 mAh/g[33]). These materials represent just a handful of those capable of delivering high specific capacities in KIBs. It is very likely that various other layered materials exist with the potential to deliver capacities comparable to those already studied. A comprehensive literature search identifies As_2S_3, found naturally as the mineral orpiment,[34] as a previously unexfoliated layered material. It is a compositional analogue of the well-known and previously exfoliated 2D materials[35] Sb_2S_3 and Bi_2S_3 and has significant potential for ion storage in battery electrodes (theoretical capacity = 1305 mAh/g, see below). However, to our knowledge, no reports exist on using it in battery electrode applications.

Although arsenic is indeed toxic, especially in its inorganic, trivalent form,[36] it is still widely used in a range of industries including textiles, wood preservation, semiconductor growth, and the production of lead-acid batteries.[37] In any case, irrespective of the possibility for its use in real applications, from the perspective of basic science, it is important to study its potential as an ion-storing electrode material. Indeed, such studies have previously been carried out on both elemental arsenic[38] and arsenic-containing compounds.[39]

In this study, we explore As_2S_3 nanosheets as an anode material for KIBs. We demonstrate that orpiment can be easily exfoliated in liquids to give nanosheets in reasonable quantities. Using single-walled carbon nanotubes as binders, As_2S_3 nanosheets can easily be solution cast into films for use as K-ion anodes. Electrochemical characterization shows these anodes to demonstrate capacities as high as 619 mAh/g and exceptional capacity retention over 1000 charge−discharge cycles.

RESULTS AND DISCUSSION

Few-Layered As_2S_3 Exfoliation and Characterization. As_2S_3 exits as a naturally occurring layered crystal, orpiment, as shown in Figure 1A.[40,41] These yellowish crystals belong to the family of 2D layered materials.[40,41] The crystal structure of As_2S_3 belongs to the space group $P2_1/n$ and has a monoclinic lattice structure.[40−44] Each single layer is made up of AsS_3 pyramids linked together by strong As−S−As covalent bonds with weak van der Waals interlayer interactions as shown in Figure 1B.[45] The unit cell contains 20 atoms distributed over two monolayers (Figure 1B).[41,44,45] An SEM image of the orpiment crystal surface, as shown in Figure 1C, confirms the layered morphology.

An orpiment crystal was first cleaned and converted to powder via bath sonication in the solvent 2-propanol (details of cleaning and liquid-phase exfoliation process are given in the Methods section). Inert atmosphere liquid-phase exfoliation (LPE) was performed by bath sonicating the resultant powder for 10 h in dried, distilled, and degassed 2-propanol under an argon atmosphere. The resultant dispersion was centrifuged to remove a large unexfoliated material (220 g) and again to remove any very small particles (3800 g) resulting in a standard dispersion (Figure 1D). The concentration (C) of the dispersion was determined to be 1 mg/mL via filtration of 1 mL of dispersion and mass weighing.

https://doi.org/10.1021/acsnano.4c03501
ACS Nano 2024, 18, 20213−20225

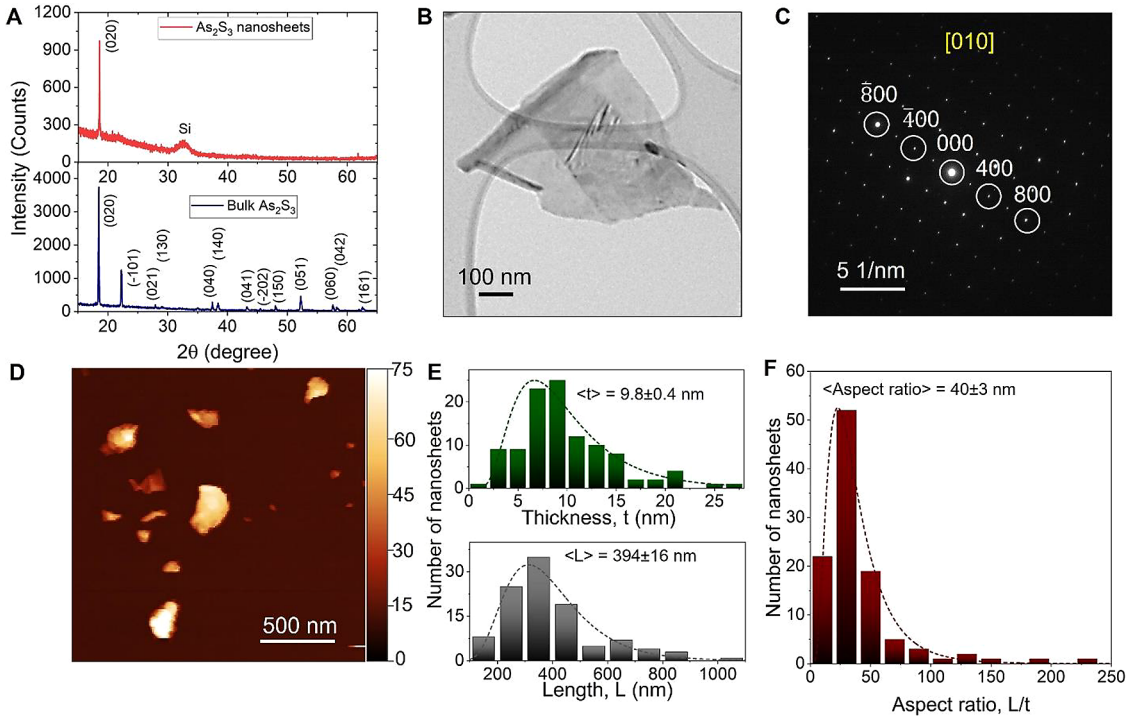

Figure 2. Structure and aspect ratio analysis of As_2S_3 nanosheets. (A) X-ray diffractogram of both the bulk crystal and exfoliated nanosheets. Diffraction peaks are indexed using PDF card number 01-071-2435 (crystal system: monoclinic, space group: $P2_1/n$). (B) TEM image of an As_2S_3 nanosheet with the corresponding SAED pattern (C). The nanosheet is oriented along the [010] direction parallel to the As_2S_3 crystal cleavage plane. A full assignment of the diffraction spot pattern can be found in the Supporting Information. (D) Atomic force microscopy image of As_2S_3 nanosheets deposited on a substrate. (E) Distribution plots illustrating the thickness and length of nanosheets. More than 100 nanosheets were individually measured for length, width, and step height, exhibiting a log-normal distribution, as indicated by the dotted curve. The aspect ratio of each nanosheet, defined as the ratio of its length to thickness, was calculated and is depicted in the distribution plot (F). The mean thickness, length, and aspect ratio are reported in the plot, along with standard errors.

To investigate the optical properties of the dispersed nanosheets, optical extinction spectroscopy was employed, as shown in Figure 1E. The extinction spectrum (Ext = −log T) was obtained and subsequently converted into an extinction coefficient spectrum (ε = Ext/Cl, where is l is the cuvette length).[46−49] As depicted in Figure 1E, the extinction coefficient spectrum exhibits a steady increase with decreasing wavelength with no clear optical absorption band-edge. The lack of a clear band-edge in nanosheet dispersions is generally due to light scattering.[48] To address this, scattering coefficient spectra (σ) were measured (Figure 1E) using an integrating sphere and then subtracted from the extinction coefficient spectrum (ε) to obtain the absorption coefficient spectrum (α).[46,48,49] The α-spectrum shows a clear band-edge at λ = 500 nm, corresponding to an optical gap of 2.5 eV. This is consistent with bandgap values of ∼2.5 eV associated with As_2S_3, as reported in the literature.[41,42,44]

Furthermore, transmission electron microscopy (TEM) was utilized to characterize the dispersion. TEM images, as presented in Figure 1F, reveal the presence of As_2S_3 nanosheets with a mean length (<L>) of approximately 350 nm. Raman spectroscopy was also employed to characterize the intermolecular vibrations. Figure 1G presents the Raman spectra of both bulk and exfoliated As_2S_3. These spectra exhibit distinct, well-defined sharp phonon modes, which can be categorized into two distinct regions: region I spans from wavenumber 120 to 210 cm^{-1}, while region II encompasses wavenumber from 280 to 390 cm^{-1}. Raman phonon peaks in region I at 135, 154, 179, and 202 cm^{-1} correspond to the bond-bending vibrations, while the phonon peaks in region II at 291, 310, 354, and 382 cm^{-1} correspond to bond-stretching vibrations.[43−45] The phonon modes of bulk and exfoliated As_2S_3 are the same within the resolution of the Raman spectrometer used in this study and are in alignment with literature data,[41,43,44] showing that exfoliation does not change the material structure. In addition, no extra Raman modes were detected, confirming that As_2S_3 nanosheets are free of impurities and did not undergo oxidation during the exfoliation process.

To gain an understanding of the crystal structure of As_2S_3 few-layered nanosheets, we employed both X-ray diffraction (XRD) and selected area electron diffraction (SAED) through TEM. Figure 2A shows the XRD pattern of the bulk crystal and exfoliated As_2S_3 nanosheets in the 2θ range from 15° to 65°. The diffraction pattern of the bulk crystal displayed several peaks at different angles, including 2θ = 18.5°, 22.2°, 28.0°, 29.0°, 37.5°, 38.4°, 43.3°, 45.3°, 48.1°, 52.3°, 57.7°, 57.9°, and 62.6°. These peaks were assigned to various hkl planes in the reciprocal lattice space of the monoclinic crystal structure of As_2S_3, such as (020), (−101), (021), (130), (040), (140), (041), (−202), (150), (051), (060), (042), and (161). It was observed that these peaks were closely aligned with the reference data for orpiment (PDF 01-071-2435), and no impurity phases were detected. A significant preferred orientation was observed, as the (0 2 0) diffraction peak was approximately three times more intense than the next highest peak, indicating that this plane is parallel to the alignment of layers along the b-axis in the orpiment crystal structure (which

https://doi.org/10.1021/acsnano.4c03501
ACS Nano 2024, 18, 20213−20225

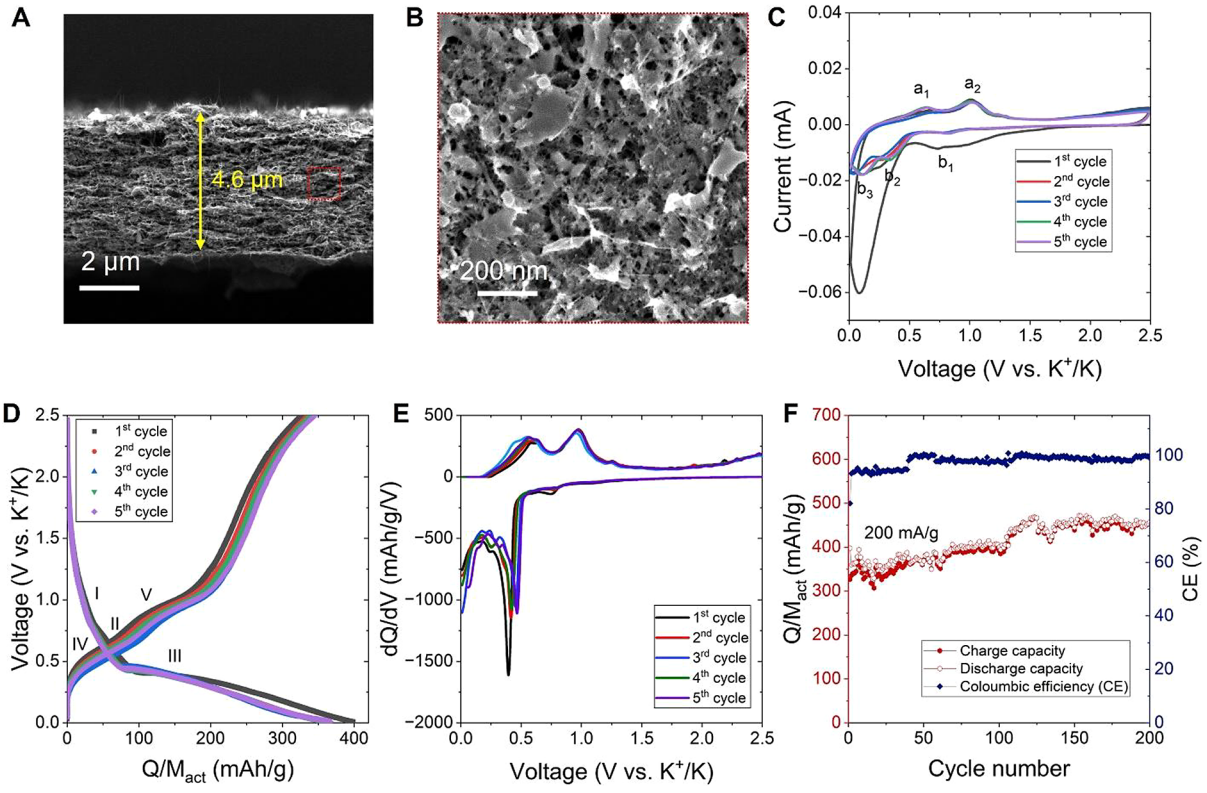

Figure 3. Investigation of the electrochemical mechanism in few-layered nanosheets of As_2S_3 (70 wt %) and CNT (30 wt %) nanocomposite anodes for KIBs. (A) Cross-sectional SEM image of the As_2S_3 electrode with a mass loading of 0.44 mg/cm^2 and a thickness of 4.6 μm. (B) SEM image revealing the interconnected network of nanosheets and carbon nanotubes on the electrode surface. (C) Initial five cycling voltammetry (CV) curves acquired at a scan rate of 0.1 mV/s. (D) Voltage profiles for the galvanostatic charge−discharge (GCD) for the first five cycles recorded at a current density of 200 mA/g and the corresponding differential voltage plots (E). (F) Charge−discharge cycling and Coulombic efficiency performance of the electrode at 200 mA/g, demonstrating an increase in specific capacity (normalized to the active mass represented as Q/M_{act}) with cycle number, plateauing after 124 cycles.

is also parallel to the cleavage plane). The highest intensity of this peak strongly suggests that the powdered sample particles predominantly took on a platelet shape, rather than a spherical form.[50] The finding is in line with similar patterns that have been previously reported in the existing literature.[51] For the exfoliated nanomaterials, the presence of only the (0 2 0) peak is a clear indication of their 2D morphology.[50] It is worth noting that the exfoliated nanosheets are not expected to perfectly restack like the bulk material, resulting in a distinct XRD pattern compared to the bulk material;[50] therefore, As_2S_3 is also expected to behave the same. The broad XRD peak at 2θ position 32.5° corresponds to the silicon (002) substrate.[52] TEM imaging of a few-layered-thick nanosheet (Figure 2B) allowed measurement of a SAED pattern (Figure 2C), showing the presence of well-defined sharp diffraction spots. The diffraction spot pattern is fully indexed (Figure S1, Supporting Information) with the monoclinic lattice structure of As_2S_3 with nanosheet orientation in the [010] direction, thus representing high crystallinity of exfoliated nanosheets of As_2S_3. Energy dispersive X-ray spectroscopy (EDX) conducted on As_2S_3 nanosheets confirms the presence of As and S elements (Figure S2, Supporting Information). Notably, oxygen is absent in the elemental EDX scans, confirming that the nanosheets formed by inert-gas LPE are anhydrous. The average atomic ratio calculated over 24 randomly selected nanoplatelets reveals <S/As> = 1.5.

Additionally, we employ atomic force microscopy (AFM) to examine the distribution of length (L), thickness (t), and aspect ratio (L/t) of exfoliated nanosheets. Figure 2D shows an AFM image displaying several nanosheets with varying sizes and thicknesses. For each individual nanosheet, length and apparent thickness were measured. Apparent thickness values were converted into real thickness (t) by measuring the step height (Figure S3, Supporting Information) as described in detail in Section A of Supporting Information. The length and thickness distribution of 100 nanosheets is presented in Figure 2E, with the mean value represented as $<L> = 394 \pm 16$ nm and $<t> = 9.8 \pm 0.4$ nm, along with standard errors. Additionally, we calculate the aspect ratio of each nanosheet by taking the ratio of length to its thickness and plot as shown in Figure 2F. The mean aspect ratio is found to be 40 ± 3, which is at the upper end for nanosheets obtained from LPE of 2D materials,[48,53] implying that the ratio of fracture (in-plane) to delamination (out-of-plane) energies is relatively large for this material.[53]

Electrochemical Storage of K^+ Ions in As_2S_3 Anodes. Previous research has consistently shown that utilizing active materials in the form of 2D nanosheets within lithium- or sodium-storing battery electrodes leads to near-theoretical capacities.[25] This is especially the case when single-walled carbon nanotubes (SWCNTs) are used as a replacement for both conductive additives and polymeric binders.[54] In this composite electrode architecture, SWCNTs establish a mechanically robust and electrically conductive network that enhances charge delivery.[54,55] This, in turn, allows for the optimization of capacity, rate capability, and cyclability.[54] We

https://doi.org/10.1021/acsnano.4c03501
ACS Nano 2024, 18, 20213−20225

anticipate that the success of this architecture for lithium- and sodium-storing electrodes can be extended to potassium storage. Due to its lower density, we might expect As_2S_3 to yield a higher specific capacity for potassium-storing anodes as compared to its analogues Sb_2S_3 (C_{theory} = 946 mAh/g) and Bi_2S_3 (C_{theory} = 625 mAh/g).[32,33] However, to our knowledge, there are no reports of Li-, Na-, or K-storing electrodes fabricated from As_2S_3. Here, we will explore the potential of nanocomposites consisting of LPE-produced As_2S_3 nanosheets and SWCNTs for developing high-performance K-ion anodes.

Nanocomposite anodes comprising As_2S_3 nanosheets and SWCNTs were fabricated for use in a half-cell configuration. In short, the dispersion of As_2S_3 nanosheets was mixed with an SWCNT dispersion in 2-propanol and then subjected to vacuum filtration onto a Celgard 2320 membrane (for detailed procedures, please refer to the Methods section). This process led to the creation of free-standing nanocomposite films (as shown in Figure S4 of Supporting Information) containing 28−30 wt % nanotubes, without the need for a polymeric binder. Subsequently, the free-standing films were cut into the required dimensions with an area of 0.178 cm^2 for electrochemical testing. The SEM image in Figure 3A, displaying the cross-sectional view of the free-standing As_2S_3@CNT electrode (total mass loading of 0.44 mg/cm^2), reveals a thickness of 4.6 μm. A magnified view of the electrode's surface, as depicted in Figure 3B, reveals a well-connected porous network of 2D nanosheets interlinked with 1D carbon nanotubes. The SEM cross-section image of the composite film, along with the corresponding elemental composition maps, is presented in Figure S4. The EDX spectra of the composite electrode indicate the presence of As and S elements. Elemental maps demonstrate a uniform distribution of As and S elements, with an expected stoichiometry of $As_2S_{3.1}$. The electrode porosity was calculated by estimating its density using the thickness and mass loading data, resulting in a density of 0.95 g/cm^3. Given the densities of As_2S_3 and SWCNT, which are 3.43 and 1.8 g/cm^3, respectively, the calculated porosity of the electrode is approximately 67%, similar to but slightly higher than nanosheet-only networks.[56]

Electrochemical characterization was carried out to assess the utility of these electrodes for potassiation/depotassiation. Figure 3C depicts the cyclic voltammograms (CV) for the first five cycles acquired at a scan rate of 0.1 mV/s in the voltage window between 0.01 and 2.5 V. The CV curve indicates that during the first discharge process, a broad cathodic peak appears at 0.75 V, mainly due to the formation of solid−electrolyte interface (SEI) films. This peak disappears in the subsequent sweep cycles. Another peak is seen at 0.08 V, which is likely associated with the alloy reactions between K and As, and is skewed by SEI formation.[57] From the second cycle, the CV curves follow similar line shapes and completely overlap demonstrating a highly reversible electrochemical reaction. During the subsequent scans, the cathodic peaks are identified in the overlapping CV curves marked as b1, b2, and b3 and located at 0.81, 0.31, and 0.12 V, respectively. Materials with the same structure are known to belong to the same family and are expected to exhibit similar characteristics. Based on the matching stoichiometry, as well as the similar structure and shape of the CV curves, it is expected that our As_2S_3 electrodes will also demonstrate consistency with the materials from the same family by displaying similar ion storage mechanisms. Therefore, it is predicted that the electrochemical reaction of As_2S_3 with potassium ion is likely to proceed similarly to that of Bi_2S_3[58] and Sb_2S_3.[32,59] During potassiation, the small cathodic peak at 0.81 V (b1) is attributed to K-ion insertion into As_2S_3. The second reduction peak at 0.31 V (b2) is assigned to a conversion reaction, i.e., electrochemical reduction of As_2S_3 to arsenic with accompanying the formation of an amorphous K_2S, and the third reduction peak centered at 0.12 V (b3) can be assigned to alloying reactions between K and arsenic. In addition, during depotassiation, two anodic peaks appearing at 0.64 V (a1) and 1.0 V (a2) can be assigned to dealloying and further reversible conversion and deintercalation reactions, respectively.[31−33,58,59]

To check the validity of the proposed mechanism, we performed galvanostatic charge−discharge (GCD) experiments on an As_2S_3@CNT electrode. Here, both charge and discharge capacities, as well as the current density, were calculated based on the active material (As_2S_3) mass and referred to as Q/M_{act}. In this study, as a part of the initial activation procedure, all electrodes were first subjected to 10 cyclic voltammograms at a scan rate of 0.1 mV/s. This is a reasonably standard activation procedure that allows the formation of an SEI layer on the electrode surface. After the activation cycles, we continued cycling the electrode for 200 charge−discharge cycles at a higher current of 200 mA/g. The voltage profiles collected for the first 5 cycles are displayed in Figure 3D with a voltage range of 0.01−2.5 V. During the discharge process, three plateau regions are noticed in the voltage range of 1.2−0.8 V (referred to as region I, indicating the intercalation process), 0.75−0.45 V (referred to as region II, indicating the conversion process), and 0.45−0.07 V (referred to as region III, indicating the alloying reaction). During the charging process, plateau region IV (0.2−0.75 V) indicates reverse conversion, while plateau region V (0.8−1.2 V) indicates reverse deintercalation reactions. The plateau regions align reasonably well with the peaks observed in the CV curves (Figure 3C).

Figure 3E shows differential voltage plots for the first 5 cycles, which are nearly identical to the peaks observed in the CV curves but slightly more well-defined. In the first cycle, the GCD curve at 200 mA/g delivers a discharge capacity of 398 mAh/g and a charge capacity of 327 mAh/g. In the subsequent cycles, charge−discharge curves are stable and remain nearly identical, indicating good stability of the nanostructures as anode materials. Figure 3F illustrates the resulting charge−discharge capacities of the As_2S_3@CNT electrodes for 200 cycles along with the Coulombic efficiencies (CEs). We consider the contribution from carbon nanotubes to the overall measured capacity of As_2S_3@CNT composite electrodes to be negligible due to their very low specific capacity (~30 mAh/g), as illustrated in the Supporting Information (Figure S5). At the beginning of cycling, the electrodes achieved a CE of 82%. During the following cycles, both the charge and discharge capacities, as well as the CE, gradually increased before reaching their maximum at around 124 cycles. At this point, the discharge and charge capacities reached 468 and 466 mAh/g, respectively, with a CE exceeding 99%. Beyond this cycle, the CE remained consistently above 99%, while the discharge and charge capacities leveled off at 459 and 457 mAh/g, respectively (refer to Figure S6, Supporting Information for the voltage profiles). These findings suggest that contrary to what was previously assumed, the electrode's activation was not fully accomplished within the first five cycles but rather necessitated over 100 cycles to reach its maximum capacity. Similar behavior was also observed by Zhou et al.[60] in their study of a

https://doi.org/10.1021/acsnano.4c03501
ACS Nano 2024, 18, 20213−20225

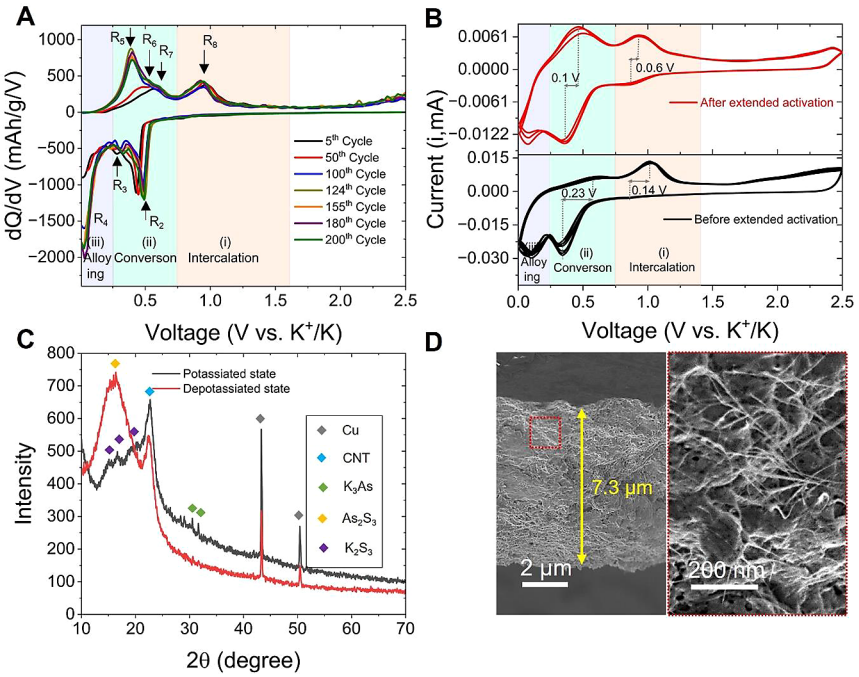

Figure 4. Postcycling analysis for studying the effect of extended activation on As_2S_3 (70 wt %) and CNT (30 wt %) nanocomposites as KIB anodes. (A) Differential voltage curves collected during the extended activation processes at a current density of 200 mA/g for 5th, 50th, 100th, 124th, 155th, 180th, and 200th cycles. (B) CV curves of the As_2S_3/CNT composite electrode before and after the extended activation processes. (C) XRD pattern of As_2S_3/CNT composite anodes in the potassiated and depotassiated states. (D) SEM images of the As_2S_3/CNT composite electrode after the extended activation processes.

KIB anode composed of VS_2 nanosheets. At 500 mA/g current, the specific capacity of the nanostructured VS_2 anode increased from 290 to 360 mAh/g after 100 cycles. However, they attributed this phenomenon to increased wetting of the electrode film by the electrolyte during cycling.[60] The cycling profile at a low current density displayed in Figure 3F demonstrates fluctuating data. This is due to the dissolution of polysulfides (that are formed during the deep potassiation process in the majority of metal sulfides) in the electrolyte and its shuttle effect results in the loss of active materials, leading to poor reversibility and fluctuating CE. Therefore, this is a significant issue associated with metal sulfides as anodes for KIBs.

To gain a thorough understanding of how activation leads to an increased capacity during cycling, the differential voltage plots were analyzed. Such plots are obtained by differentiating the GCD curves (i.e., those used to prepare Figure 3F) and plotted as dQ/dV versus voltage. Figure 4A shows the dQ/dV versus voltage plot for selected cycles for the 5th, 50th, 100th, 124th, 155th, 180th, and 200th at a current density of 200 mA/g. The curves collected at different cycles show a noticeable difference compared to the curve collected at cycle 5. However, after the 124th cycle, all curves overlap each other. This indicates that the activation process is complete after the 124th cycle, and the material remains electrochemically stable thereafter.

Following recent research by Nithya et al.,[58] we propose that the electrode undergoes the following reactions at various stages of potential, which we divide into three regions as shown in Figure 4A:

During potassiation:

Region I: at 1.4−0.75 V (intercalation process)

$$As_2S_3 + xK^+ + xe^- \rightarrow K_xAs_2S_3 \quad (1)$$

Region II: at 0.75−0.25 V (conversion reactions)

$$K_xAs_2S_3 + (2 - x)K^+ + (2 - x)e^- \rightarrow K_2S_3 + 2As \quad (2)$$

$$K_2S_3 + 4K^+ + 4e^- \rightarrow 3K_2S \quad (3)$$

Region III: at 0.25−0.01 V (alloying reactions)

$$2As + 6K^+ + 6e^- \rightarrow 2K_3As \quad (4)$$

Overall, this reaction is equivalent to

$$As_2S_3 + 12K^+ + 12e^- \rightarrow 3K_2S + 2K_3As \quad (5)$$

In Figure 4A, two redox peaks are observed in region (ii), indicating that the conversion reaction occurs in two main steps.[61] The first step (eq 2) involves the creation of amorphous arsenic nanoparticles by reducing As_2S_3 into As and forming K_2S_3 polysulfide (peak R_2 in Figure 4A). These nanosized As particles possess a robust ability to effectively trap the discharge products, thereby preventing the shuttling of byproducts in the electrode surface.[62] Consequently, the subsequent reactions (eqs 3 and 4) are accelerated, which is expected to enhance the formation of K_3As; this is clearly seen in Figure 4A as the R_4 peak corresponding to K_3As alloy intensifies with cycling, remaining stable after 124 cycles. During the charging process, which is also known as depotassiation, the reactions take place reversibly, and the discharge products are consumed to regenerate the original materials. Figure 4A clearly displays these reactions; peak R_5 indicates dealloying at 0.39 V, while the R_6 and R_7 peaks show reverse conversion reactions at 0.48 and 0.58 V. Peak R_8 represents the deintercalation reaction at 0.96 V. In addition, we notice some peak shifts in the dQ/dV curves, and the sharpening of the dealloying peak during the activation has a substantial influence on enhanced charge storage.

https://doi.org/10.1021/acsnano.4c03501
ACS Nano 2024, 18, 20213−20225

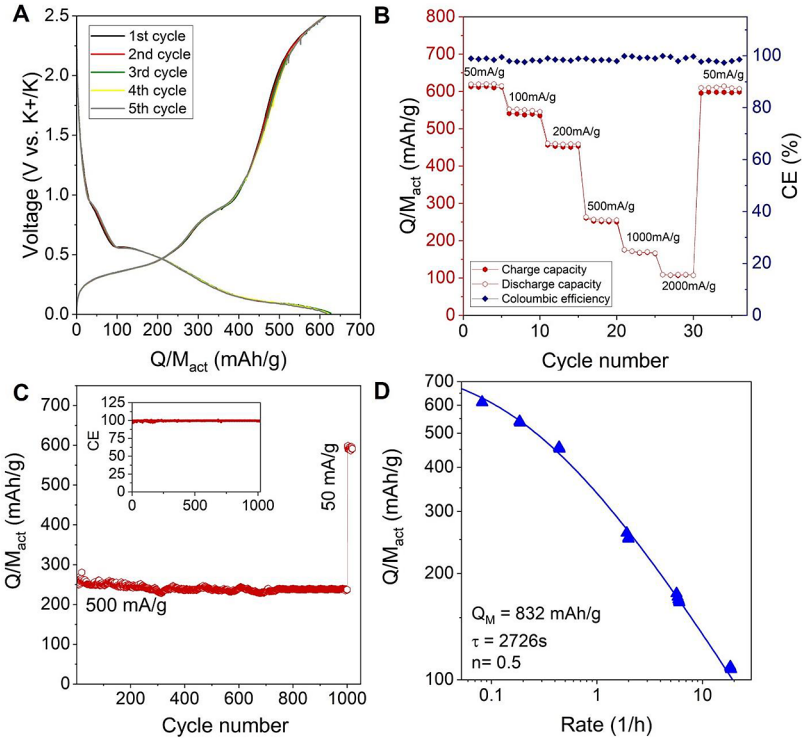

Figure 5. Electrochemical properties of the few-layered As_2S_3@CNT electrode. (A) Discharge and charge curves at 50 mA/g for the initial five cycles after extended electrode activation. (B) Rate capability of the electrode at different current densities. (C) Long cycling performance at 500 mA/g. The inset shows the CE (%) with cycle number. (D) Specific capacity plotted versus rate, R ($R = (I/M_{Act})/(Q/M_{Act})$), for the electrode. The fit is to eq 1 with the fit parameters given in the panel.

To validate our findings, postmortem analysis of As_2S_3 battery electrodes was performed, and the results have been presented in both Figures 4 and S6. To begin, we examined the CV curves of the As_2S_3@CNT anodes before and after 200 activation cycles to quickly detect any changes in their electrochemical storage properties. The analysis revealed significant changes, as shown in Figure 4B. After extended activation, the voltage hysteresis between conversion and deconversion peaks is reduced to 0.1 V, while intercalation and deintercalation peaks are reduced to 0.06 V. This leads to better reversible electrochemical charge storage, resulting in an enhanced electrochemical K-ion storage capacity. The findings suggest that the discharge products (K_2S_3 and K_2S) can be efficiently trapped by highly active, ultrafine As particles formed in eq 2, which significantly reduces the shuttle effect and leads to excellent K-ion charge storage.[63] Thus, we predict that during activation, amorphous arsenic nanoparticles play a vital role in realizing enhanced charge storage in the charge/discharge process. To evaluate the structural changes in the activated electrode, we performed ex situ X-ray diffractograms in the potassiated and depotassiated states of the electrode (Figure 4C). In the potassiated state, the electrode displayed XRD peaks corresponding to the presence of K_3As and K_2S_3 phases, whereas in the depotassiated state, the XRD pattern showed peaks corresponding to only As_2S_3 and CNT, indicating that the structure of the As_2S_3 in As_2S_3@CNT anodes remains unchanged after cycling. This confirms the above redox reactions of As_2S_3 with K ions,[61] implying that a charge equivalent to 12 electrons can be stored per formula unit of As_2S_3. Thus, the theoretical capacity of As_2S_3 is calculated to be 1305 mAh/g.

To investigate the morphological changes in the activated electrode, we employed SEM imaging. As depicted in Figure 4D, the cross-sectional view of the electrode revealed a clear expansion of from 4.6 to 7.3 μm after 200 cycles. This expansion indicates a reduction in density from 0.95 to 0.6 g/cm^3, which in turn implies an increase in porosity from 67 to 79% and internal surface area. After cycling, the electrodes appear smoother with no visible 2D platelets indicating a uniform and amorphous structure. It is observed that the conversion-type materials undergo shape alteration upon cycling, and it is highly unlikely for them to retain their original morphology after cycling (Figure 4D). The ex situ XRD pattern of the electrode, which was activated for 200 cycles (see Figure S7), revealed a distinctive broad diffraction peak located at diffraction angles 2θ between 10° and 21°. The presence of this broad peak is a compelling indicator of medium-range ordering in noncrystalline structures of As_2S_3.[64] This confirmed the transition of As_2S_3 from the crystalline to noncrystalline phase. It is worth noting that the observed phenomena are in line with the established literature that highlights the amorphization process occurring in both alloy and conversion-type materials during extended cycling, ultimately resulting in the formation of amorphous materials.[65] After 200 cycles, SEM-EDX elemental maps were used to analyze the distribution of As and S elements in the cross-sectional film of the As_2S_3/CNT composite electrode to demonstrate its structural stability (Figure S8). After cycling, the electrodes exhibited the distribution of As and S elements, as well as the distribution of K, P, and F from the electrolyte.

After the 200 cycles shown in Figure 3F, we performed five charge−discharge cycles at a current density of 50 mA/g, and the resulting voltage profiles are displayed in Figure 5A. The

https://doi.org/10.1021/acsnano.4c03501
ACS Nano 2024, 18, 20213−20225

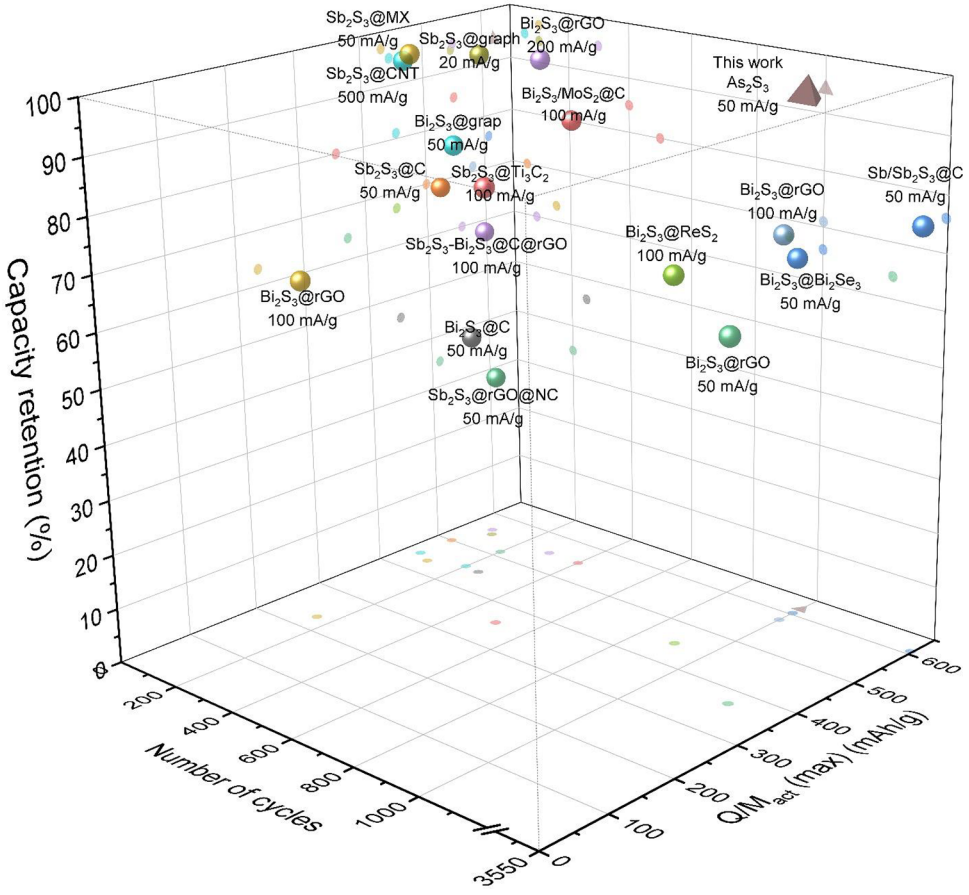

Figure 6. Comparative analysis of maximum specific capacity (Q/M_{act} (max)), cycle number, and capacity retention between the finding of this study and those reported for Sb_2S_3 and Bi_2S_3 in the literature. For list of references, refer to Table S2 in the Supporting Information.

overlapping of voltage profiles confirmed a highly reversible electrochemical reaction, signifying the electrode's ability to repeatedly transition between charge and discharge states without substantial performance degradation. Notably, we achieved an average discharge capacity of 619 mAh/g and an average charge capacity of 612 at 50 mA/g. To comprehensively evaluate the performance, rate-performance tests were performed to assess its capacity and efficiency at different current densities, as depicted in Figure 5B. The data demonstrate the expected falloff in capacity with increasing current. However, when the current density was reduced back to 50 mA/g, an average discharge capacity of 610 mA/g was obtained, indicating excellent reversibility. The impressive nature of As_2S_3 nanosheets lies in their ability to offer a high specific capacity and exceptional reversibility. It is important to emphasize that this low-rate specific capacity exceeds that of almost all other reported 2D materials utilized in KIB anodes across the existing literature (see Table 1, Supporting Information). The only higher values we know of are 860 mAh/g (50 mA/g) for $MoS_{1.5}Se_{0.5}$-based electrodes.[66] Furthermore, the cell consistently maintains a CE exceeding 98% across all tested current densities, indicative of efficient charge transfer and minimal side reactions. This underscores the cell's capability to mitigate parasitic reactions and prevent capacity degradation.

To assess the cell durability, we examined capacity retention under relatively high current density conditions, subjecting the cell to 1000 charge−discharge cycles at 500 mA/g. As shown in Figure 5C, the initial discharge capacity at the beginning of cycling was 253 mAh/g, gradually decreasing to 237 mAh/g after 1000 cycles. This demonstrated an impressive capacity retention of 94% for this electrode. Notably, this level of retention is exceptional among anodes for KIBs based on 2D materials (refer to Table S1 in the Supporting Information) and is higher than that of similar materials such as Sb_2S_3- and Bi_2S_3-based KIB anodes (refer to Table S2 in the Supporting Information). A detailed comparison of the stability and capacity of As_2S_3@CNT anodes with other 2D material-based KIB anodes is presented in Table S1 and with other sulfide-based anodes in Table S2. The electrochemical performance of our As_2S_3@CNT anodes is assessed in Figure 6 by plotting the maximum specific capacity (Q/M_{Act}) against the capacity retention and cycle number. Our As_2S_3@CNT anodes exhibit competitive capacity and stability after long cycling when compared to the best-reported results for electrodes based on As_2S_3 analogues, Sb_2S_3, and Bi_2S_3 for KIB. These findings underscore its robust nature and enduring electrochemical performance characteristics. Moreover, when the current density was reduced back to 50 mA/g after 1000 cycles at 500 mA/g, an average discharge capacity of 593 mA/g was obtained, again indicating excellent reversibility and superior potassium storage with greater stability. To achieve sustainable, safe, and long-lasting KIBs, the use of ether-based electrolytes is promising. By using either green ether-based electrolytes or specific molecular-designed phosphate-based electrolytes, we can significantly enhance the reliability and stability of our electrodes.[67−69]

https://doi.org/10.1021/acsnano.4c03501
ACS Nano 2024, 18, 20213−20225

Quantitative Analysis of Rate Performance. Previously, we have shown that one can extract information about the ultimate capacity of electrodes, as well as quantifying the rate performance, via quantitative analysis of capacity versus rate data.[70−73] This involves plotting the measured specific capacity (Q/M_{Act}) versus charge/discharge rate as shown in Figure 5D. For such analysis, we represent charge/discharge rate via a parameter, R, which is defined as $R = I/Q$, i.e., the specific current divided by the specific capacity measured at that current.[70,71,73−75] This is useful because $1/R$ is a measure of the actual charge/discharge time of the electrode at a given current. This graph shows Q/M_{Act} to decay with rate (R) as is usually observed.[72,73]

Such data can be analyzed using various semiempirical fitting equations,[76] such as that proposed recently by our group:[73]

$$Q/M_{Act} = Q_{M,Act}[1 - (R\tau)^n(1 - e^{-(R\tau)^{-n}})] \quad (6)$$

Here, fitting yields three fit parameters: $Q_{M,Act}$, which is the capacity (normalized to active mass) at an infinitely low rate; τ, the characteristic charge/discharge time; and n, a parameter that indicates whether diffusive (n = 0.5) or capacitive (electrical) (n = 1) limitations dominate rate performance.[70−74] As shown in Figure 5D, this equation fits the experimental data extremely well with the following fit values: $Q_{M,Act}$ = 832 ± 36 mAh g^{-1}, n = 0.50 ± 0.01, and τ = 2726 ± 360 s. We will discuss these fit parameters one by one.

The $Q_{M,Act}$ value represents the maximum achievable capacity, measured at an infinitely low rate. The fit value (832 ± 36 mAh g^{-1}) was about two-thirds of the theoretical capacity (1305 mAh/g). This is somewhat lower than previous results which show that exfoliating layered materials to nanosheets which are then combined with carbon nanotubes to yield composite electrodes allows almost full utilization of the active material for storage of Li, Na, and K ions.[77−81] However, it is consistent with our literature review data (Figure 6 and Table S2), which show Sb_2S_3-based K-storing electrodes to display 37−65% of theoretical capacity, although Bi_2S_3-based K-storing electrodes showed somewhat higher values (up to 93% of theoretical capacity).

In addition, the n-value is exactly equal to 0.5, indicating that our electrodes are diffusion-limited, at least for these thin electrodes (∼7 μm after cycling). Probably the most useful parameter is the time constant, τ. This represents the minimum charge−discharge time for the electrode and can be used as a metric for rate performance with higher values of τ indicating poorer rate performance. Our τ-value (2736 s) is large, comparable with the largest reported for 2D-based Li- or Na-ion batteries (ref 72 shows the reported range to be roughly 1 s < τ < 10,000 s). This indicates very poor rate performance. However, we note that rate performance in general and the time constant in particular depend very strongly on electrode thickness.[70,72,73] Previously, we proposed that a reasonable figure of merit for rate performance is τ/L_E^2, where L_E is the electrode thickness, with large values indicating poor rate performance.[72,73] This parameter removes some (but not all) of the thickness dependence of τ, especially for electrodes with practically relevant thicknesses (>20 μm). Taking the postcycling value of L_E = 7.3 μm yields $\tau/L_E^2 = 5 \times 10^{13}$ s/m^2. Comparing this to the summary over many Li- and Na-storing materials reported in ref 72 shows this value to be very high for this electrode thickness, indicating that As_2S_3 electrodes have some property that dramatically limits rate performance. Given that the value of n = 0.5 indicates diffusion limitations, it is suggested that the main culprit might be solid-state diffusion in the nanosheets. The time scale associated with solid-state diffusion is roughly $\tau_{SSD} = L_{AM}^2/D_{AM}$, where L_{AM} is the diffusion length and D_{AM} is the (in-plane) diffusion coefficient within the interlayer channel. Assuming that τ is dominated by the solid-state diffusion time, we can approximate $\tau_{SSD} = L_{AM}^2/D_{AM}\tilde{\tau}$. Because τ is the sum of all possible time scales limiting rate performance,[73] this equation defines the maximum possible value of τ_{SSD}. Taking L_{AM} ∼ 200 nm (ions only need to diffuse from the edge to the center of the nanosheets), this means D_{AM} is slightly larger than 1.5×10^{-17} m^2/s. This is somewhat smaller than the value of $\sim 10^{-15}$ m^2/s reported for K^+ diffusion in Sb_2S_3.[31] Compared to the expected range of D_{AM} values for Li and Na ions in 2D materials ($\sim 10^{-19}-10^{-13}$ m^2/s),[72] these values are not particularly high, indicating that As_2S_3 (or indeed Sb_2S_3) is not best suited to achieving good rate performance. However, we note that this may not be such a problem in electrodes with practically relevant thickness (∼100 μm). Then, liquid-phase diffusion becomes dominant,[70] rendering solid-state diffusion much less important. Such a transition was recently mapped out for sodium-storing electrodes based on red phosphorus.[79]

CONCLUSIONS

In this study, we successfully achieved the exfoliation of layered As_2S_3 and fully characterized the resulting few-layered nanosheets. Combined AFM and TEM measurements showed the nanosheets to be of a high aspect ratio and of excellent quality. Raman spectroscopy and XRD analysis showed the nanosheet structure to be identical to that of bulk and confirmed the absence of impurities and oxides in the nanosheets.

Electrochemical characterization of As_2S_3 nanosheets as KIB anodes revealed exceptional K-storage behavior, achieving a capacity of 619 mAh/g at a current density of 50 mA/g. The electrodes demonstrated excellent cyclability, achieving a CE exceeding 99% after an initial activation process. The ex situ XRD provided support for our proposed electrochemical mechanism, affirming the storage of a charge equivalent to 12 electrons per formula unit of As_2S_3. This calculation indicated a theoretical capacity of 1305 mAh/g. Furthermore, our As_2S_3@CNT electrode displayed an outstanding capacity retention of 94% after 1000 cycles at a high current density of 500 mA/g. This combination of capacity and stability after long cycling is competitive with the very best results reported for electrodes based on As_2S_3 analogues and Sb_2S_3- and Bi_2S_3-based KIB anodes as displayed in Figure 6. The quantitative analysis of capacity versus rate data highlighted a close correspondence between the maximum achievable capacity (832 mAh/g) and theoretical capacity, affirming the complete utilization of active materials for ion storage. Nonetheless, we did observe a notable limitation in the rate performance, which we attributed to solid-state diffusion constraints within the nanosheets. Our analysis of electrode thickness-dependent parameters pointed to a relatively small diffusion coefficient within the interlayer channels.

We believe that the impressive theoretical capacity, high efficiency, and substantial capacity retention of these nanosheets position them as promising candidates for cutting-edge KIB applications. Future research endeavors can delve deeper into the rate performance challenges and work toward

https://doi.org/10.1021/acsnano.4c03501
ACS Nano 2024, 18, 20213−20225

unlocking the full potential of these nanosheets for practical energy storage applications.

METHODS

Exfoliation. The As_2S_3 crystal was ground into chunks of powder, which was bath-sonicated in 2-propanol for 30 min at a frequency of 37 MHz at ambient temperature. This results in a light-yellow dispersion, with chunks of powder at the bottom of the vial, which were collected for the inert LPE procedure. This step ensures the removal of any surface impurities if present. For the inert-gas exfoliation LPE process, the cleaned chunks of powder were bath-sonicated in an argon atmosphere for 10 h in dried, distilled, and degassed 2-propanol. The initial starting concentration was kept at 2 mg/mL. A round-bottom flask was used in the sonication process (Branson ultrasonic bath, CPX2800-E, 130 W). The dispersion was cooled periodically by exchanging the bath water with ice-cooled water every 30 min to maintain a temperature < 10 °C. Following sonication, the obtained dispersion underwent two consecutive centrifugation steps. The first step involved centrifugation at 220 g for 2 h aimed at removing large and thick unexfoliated particles. The supernatant obtained after this step was separated from the sediment under an inert atmosphere and subjected to a second centrifugation step at 3800 g for 3 h. This step ensures the removal of impurities and defective nanomaterials that are typically present in the supernatant at higher speeds, leaving pristine few-layered nanosheets in the sediment. The sediment was then redispersed in a fresh 2-propanol solvent, and the concentration was carefully measured. This is referred to as a standard sample.

Electrode Formation. In the first step, a dispersion of SWCNTs was prepared in 2-propanol with the goal of achieving a concentration of <0.1 mg/mL to prevent nanotube aggregation in the obtained dispersion. To achieve this, 8 mg of P3-SWCNTs were suspended in 80 mL of 2-propanol, and the resulting solution underwent probe sonication for 3 h using a horn-tip sonic probe (Vibracell CVX, 750W). The amplitude was set at 50% with a pulse duration of 6 s on/2 s off. The temperature was carefully maintained at <10 °C throughout the probe sonication process by employing ice-cooling. The outcome of this process was a black dispersion, which was allowed to free-stand for 2 h. Afterward, the top two-thirds of the dispersion was separated, and its final concentration was measured via filtering, resulting in a concentration of 0.085 mg/mL. In the second step, the standard exfoliated dispersion of As_2S_3 was mixed with the SWCNT dispersion in the weight ratio of 70:30 and was bath-sonicated for 30 min to ensure uniform mixing. In the final step, the resultant mixture was vacuum-filtered using the Celgard 2320 membrane with a thickness of 20 μm and an area of 2 cm^2. This resulted in a free-standing nanocomposite film that would be utilized as an electrode. This resultant film was subsequently cut into an area of 0.178 cm^2, which was required for electrochemical testing. The areal mass loading of As_2S_3 electrodes was calculated by using the thickness obtained from SEM cross-sectional measurements, along with the area and mass of the electrode, yielding a value of 0.44 mg/cm^2.

Assembly of K-Ion Half Cells. K-ion half cells were assembled using CR-2032 type coin cells (14 mm; MTI Corp.) in a glovebox filled with argon, ensuring O_2 and H_2O levels were maintained below 0.1 ppm. Potassium metal pieces, initially soaked in mineral oil within the glovebox, were wiped clean to remove the oil. Subsequently, the metal pieces were cut and sliced with a blade to expose fresh metal surfaces and then rolled into flat discs for use as counter/reference electrodes. Whatman glass fiber filters (GD/D, diameter 90 mm) were employed as separators. The electrolyte consisted of potassium bis(fluorosulfonyl)imide (KFSI, 2 M) dissolved in triethyl phosphate (TEP). After assembly within the glovebox, the cells were removed and placed in an oven at 40 °C for 24 h before conducting electrochemical measurements.

Characterization. The UV−visible extinction and absorption measurements were conducted using a PerkinElmer Lambda 1050 spectrometer within the wavelength range of 250−800 nm. Quartz cuvettes with a 4 mm path length were employed for this purpose. The concentration of the dispersion was determined by filtering and weighing membranes (Celgard 2320) to calculate the extinction coefficient spectra. For the absorbance spectra, a setup utilizing an integration sphere with a radius of 150 mm was employed. TEM imaging was performed using a JEOL 2100 instrument on holey carbon grids (400 mesh) with an accelerating voltage of 200 kV. High-resolution TEM and SAED were carried out using an FEI TITAN G2 80−300 microscope operated in STEM mode at 300 kV acceleration. Multiframe ADF STEM image series were recorded using the Fischione model 3000 ADF detector before rigid and nonrigid registration using the SmartAlign software from HREM Research (Tokyo).

XRD spectra were obtained with a Bruker D8 Discover high-resolution diffractometer equipped with a copper tube emitting K_α radiation (wavelength of 1.5406 Å) and a double-bounce Ge [220] monochromator. The spectra were acquired in the 2θ range from 10 to 80° on films prepared on silicon (100) wafers and on electrodes (fresh free-standing electrode, electrode on Cu foil after it has run 200 GCD cycles, and electrodes which are potassiated and depotassiated to different voltages).

Raman spectroscopy was conducted using a Horiba Jobin Yvon LabRAM ARAMIS instrument in ambient conditions, both on bulk crystals and films made on silicon wafers by a drop-cast method using dispersion containing nanosheets. A 532 nm laser with adjustable power was used to excite the samples with a 100× objective. A grating with 1800 grooves per millimeter dispersed the signal onto the CCD detector maintained at −70 °C. Samples were prepared by drop-casting dispersion onto silicon wafers, which are heated at 50 °C.

AFM was carried out using a Bruker multimode 8 microscope in ScanAsyst mode, employing an OLTESPA R3 cantilever. The samples for AFM are prepared by drop casting a diluted dispersion on silicon wafers and heating it at 60 °C, followed by drying using argon gas.

Scanning electron microscopy (SEM) was performed using a Carl ZEISS Ultra Plus SEM. Samples were mounted on aluminum SEM stubs using conductive carbon tabs (Ted Pella) and grounded using conductive silver paint (PELCO, Ted Pella). All images were captured at an accelerating voltage of 2 kV by using a working distance of 5 mm and a 30 μm aperture. Both the Inlens and SE2 detectors were used for imaging. EDX analysis was performed using a 20 mm^2 Oxford INCA EDX detector. Cross-sectional SEM images of battery electrodes were taken pre- and postcycling by fracturing the free-standing electrodes. The average electrode thickness was determined by measuring the electrode thickness from SEM cross sections across the electrode.

ASSOCIATED CONTENT

Supporting Information

The Supporting Information is available free of charge at https://pubs.acs.org/doi/10.1021/acsnano.4c03501.

SAED pattern, EDX, and step-height analysis of exfoliated nanosheets of As_2S_3; electrochemical performance of the SWCNT electrode, postcycling analysis of free-standing As_2S_3@CNT electrodes, and voltage profiles; and literature comparison of this work with others (PDF)

AUTHOR INFORMATION

Corresponding Author

Jonathan N Coleman − *School of Physics, CRANN & AMBER Research Centres, Trinity College Dublin, Dublin 2 D02 E8C0, Ireland;* orcid.org/0000-0001-9659-9721; Phone: +353 (0) 1 8963859; Email: colemaj@tcd.ie

https://doi.org/10.1021/acsnano.4c03501
ACS Nano 2024, 18, 20213−20225

Authors

Harneet Kaur − *School of Physics, CRANN & AMBER Research Centres, Trinity College Dublin, Dublin 2 D02 E8C0, Ireland;* orcid.org/0000-0002-5349-6770

Bharathi Konkena − *School of Physics, CRANN & AMBER Research Centres, Trinity College Dublin, Dublin 2 D02 E8C0, Ireland;* orcid.org/0000-0001-6010-4547

Mark McCrystall − *School of Physics, CRANN & AMBER Research Centres, Trinity College Dublin, Dublin 2 D02 E8C0, Ireland;* orcid.org/0000-0001-9262-589X

Kevin Synnatschke − *School of Physics, CRANN & AMBER Research Centres, Trinity College Dublin, Dublin 2 D02 E8C0, Ireland;* orcid.org/0000-0001-7018-9396

Cian Gabbett − *School of Physics, CRANN & AMBER Research Centres, Trinity College Dublin, Dublin 2 D02 E8C0, Ireland*

Jose Munuera − *School of Physics, CRANN & AMBER Research Centres, Trinity College Dublin, Dublin 2 D02 E8C0, Ireland;* orcid.org/0000-0002-8176-4795

Ross Smith − *School of Physics, CRANN & AMBER Research Centres, Trinity College Dublin, Dublin 2 D02 E8C0, Ireland*

Yumei Jiang − *School of Physics, CRANN & AMBER Research Centres, Trinity College Dublin, Dublin 2 D02 E8C0, Ireland*

Raman Bekarevich − *School of Chemistry, CRANN & AMBER Research Centres, Trinity College Dublin, Dublin 2 D02W9K7, Ireland*

Lewys Jones − *School of Physics, CRANN & AMBER Research Centres, Trinity College Dublin, Dublin 2 D02 E8C0, Ireland*

Valeria Nicolosi − *School of Chemistry, CRANN & AMBER Research Centres, Trinity College Dublin, Dublin 2 D02W9K7, Ireland;* orcid.org/0000-0002-7637-4813

Complete contact information is available at: https://pubs.acs.org/10.1021/acsnano.4c03501

Author Contributions

[§]B.K. and M.M. contributed equally to this work.

Notes

The authors declare no competing financial interest.

ACKNOWLEDGMENTS

The authors extend their gratitude to the European Commission for their support, notably the Graphene Flagship (Core 2 and Core 3 grant agreement number: 785219 and 881603, respectively), as well as the 2D-PRINTABLE project. B.K. acknowledges research funding from the Science Foundation Ireland (SFI)-IRC pathway program (grant number 22/PATH-S/10706). Acknowledgement is made to the Science Foundation Ireland (SFI) for funding the AMBER center (SFI/12/RC/2278_P2) and for providing facilities in the SFI-funded AML and ARL laboratories. C.G. acknowledges research supported by the European Union through the Horizon Europe project 2D-PRINTABLE (GA-101135196).

REFERENCES

(1) Liang, Y.; Zhao, C. Z.; Yuan, H.; Chen, Y.; Zhang, W.; Huang, J. Q.; Yu, D.; Liu, Y.; Titirici, M. M.; Chueh, Y. L. A review of rechargeable batteries for portable electronic devices. *InfoMat* **2019**, *1* (1), 6−32.

(2) Eftekhari, A. *Lithium Batteries for Electric Vehicles: From Economy to Research Strategy*. ACS Publications, 2019.

(3) Diouf, B.; Pode, R. Potential of lithium-ion batteries in renewable energy. *Renewable Energy* **2015**, *76*, 375−380.

(4) Zubi, G.; Dufo-López, R.; Carvalho, M.; Pasaoglu, G. The lithium-ion battery: State of the art and future perspectives. *Renew. Sustain. Energy Rev.* **2018**, *89*, 292−308.

(5) Christmann, P.; Gloaguen, E.; Labbé, J.-F.; Melleton, J.; Piantone, P. Global Lithium Resources and Sustainability Issues. In *Lithium Process Chemistry*, Elsevier, 2015; pp 1−40.

(6) Peters, J. F.; Weil, M. A critical assessment of the resource depletion potential of current and future lithium-ion batteries. *Resources* **2016**, *5* (4), 46.

(7) Zhang, W.; Lu, J.; Guo, Z. Challenges and future perspectives on sodium and potassium ion batteries for grid-scale energy storage. *Mater. Today* **2021**, *50*, 400−417.

(8) Mohan, I.; Raj, A.; Shubham, K.; Lata, D. B.; Mandal, S.; Kumar, S. Potential of potassium and sodium-ion batteries as the future of energy storage: Recent progress in anodic materials. *J. Energy Storage* **2022**, *55*, No. 105625.

(9) Kubota, K.; Dahbi, M.; Hosaka, T.; Kumakura, S.; Komaba, S. Towards K-ion and Na-ion batteries as "beyond Li-ion. *Chem. Record* **2018**, *18* (4), 459−479.

(10) Biemolt, J.; Jungbacker, P.; van Teijlingen, T.; Yan, N.; Rothenberg, G. Beyond lithium-based batteries. *Materials* **2020**, *13* (2), 425.

(11) Liu, Y.; Liu, X.; Wang, T.; Fan, L.-Z.; Jiao, L. Research and application progress on key materials for sodium-ion batteries. *Sustainable Energy & Fuels* **2017**, *1* (5), 986−1006.

(12) Bin, D.; Wang, F.; Tamirat, A. G.; Suo, L.; Wang, Y.; Wang, C.; Xia, Y. Progress in aqueous rechargeable sodium-ion batteries. *Adv. Energy Mater.* **2018**, *8* (17), No. 1703008.

(13) Rajagopalan, R.; Tang, Y.; Ji, X.; Jia, C.; Wang, H. Advancements and challenges in potassium ion batteries: a comprehensive review. *Adv. Funct. Mater.* **2020**, *30* (12), No. 1909486.

(14) Pramudita, J. C.; Sehrawat, D.; Goonetilleke, D.; Sharma, N. An initial review of the status of electrode materials for potassium-ion batteries. *Adv. Energy Mater.* **2017**, *7* (24), No. 1602911.

(15) Zhang, X.; Yang, D.; Rui, X.; Yu, Y.; Huang, S. Advanced cathodes for potassium-ion battery. *Curr. Opin. Electrochem.* **2019**, *18*, 24−30.

(16) Zheng, J.; Wu, Y.; Sun, Y.; Rong, J.; Li, H.; Niu, L. Advanced anode materials of potassium ion batteries: from zero dimension to three dimensions. *Nano-Micro Lett.* **2021**, *13*, 1−37.

(17) Chen, K. S.; Balla, I.; Luu, N. S.; Hersam, M. C. Emerging Opportunities for Two-Dimensional Materials in Lithium-Ion Batteries. *ACS Energy Lett.* **2017**, *2* (9), 2026−2034.

(18) Liu, Q.; Hu, Z.; Chen, M.; Zou, C.; Jin, H.; Wang, S.; Chou, S. L.; Dou, S. X. Recent progress of layered transition metal oxide cathodes for sodium-ion batteries. *Small* **2019**, *15* (32), No. 1805381.

(19) Zhang, C.; Pan, H.; Sun, L.; Xu, F.; Ouyang, Y.; Rosei, F. Progress and perspectives of 2D materials as anodes for potassium-ion batteries. *Energy Storage Mater.* **2021**, *38*, 354−378.

(20) Miró, P.; Audiffred, M.; Heine, T. An atlas of two-dimensional materials. *Chem. Soc. Rev.* **2014**, *43* (18), 6537−6554.

(21) Coleman, J. N.; Lotya, M.; O'Neill, A.; Bergin, S. D.; King, P. J.; Khan, U.; Young, K.; Gaucher, A.; De, S.; Smith, R. J. Two-dimensional nanosheets produced by liquid exfoliation of layered materials. *Science* **2011**, *331* (6017), 568−571.

(22) Nicolosi, V.; Chhowalla, M.; Kanatzidis, M. G.; Strano, M. S.; Coleman, J. N. Liquid exfoliation of layered materials. *Science* **2013**, *340* (6139), No. 1226419.

(23) Backes, C.; Szydlowska, B. M.; Harvey, A.; Yuan, S. J.; Vega-Mayoral, V.; Davies, B. R.; Zhao, P. L.; Hanlon, D.; Santos, E. J. G.; Katsnelson, M. I.; et al. Production of Highly Monolayer Enriched Dispersions of Liquid-Exfoliated Nanosheets by Liquid Cascade Centrifugation. *ACS Nano* **2016**, *10* (1), 1589−1601.

(24) Chen, K.-S.; Balla, I.; Luu, N. S.; Hersam, M. C. Emerging opportunities for two-dimensional materials in lithium-ion batteries. *ACS Energy Lett.* **2017**, *2* (9), 2026−2034.

(25) Peng, L.; Zhu, Y.; Chen, D.; Ruoff, R. S.; Yu, G. Two-dimensional materials for beyond-lithium-ion batteries. *Adv. Energy Mater.* **2016**, *6* (11), No. 1600025.
(26) Pomerantseva, E.; Gogotsi, Y. Two-dimensional heterostructures for energy storage. *Nature Energy* **2017**, *2* (7), No. 17089.
(27) Sultana, I.; Rahman, M. M.; Ramireddy, T.; Chen, Y.; Glushenkov, A. M. High capacity potassium-ion battery anodes based on black phosphorus. *J. Mater. Chem. A* **2017**, *5* (45), 23506−23512.
(28) Fang, L.; Xu, J.; Sun, S.; Lin, B.; Guo, Q.; Luo, D.; Xia, H. Few-layered tin sulfide nanosheets supported on reduced graphene oxide as a high-performance anode for potassium-ion batteries. *Small* **2019**, *15* (10), No. 1804806.
(29) Jia, B.; Yu, Q.; Zhao, Y.; Qin, M.; Wang, W.; Liu, Z.; Lao, C. Y.; Liu, Y.; Wu, H.; Zhang, Z. Bamboo-like hollow tubes with MoS2/N-doped-C interfaces boost potassium-ion storage. *Adv. Funct. Mater.* **2018**, *28* (40), No. 1803409.
(30) Yao, K.; Xu, Z.; Ma, M.; Li, J.; Lu, F.; Huang, J. Densified metallic MoS2/graphene enabling fast potassium-ion storage with superior gravimetric and volumetric capacities. *Adv. Funct. Mater.* **2020**, *30* (24), No. 2001484.
(31) Zhang, P.; Zhu, Q.; Wei, Y.; Xu, B. Achieving stable and fast potassium storage of Sb2S3@ MXene anode via interfacial bonding and electrolyte chemistry. *Chem. Eng. J.* **2023**, *451*, No. 138891.
(32) Cheng, Y.; Yao, Z.; Zhang, Q.; Chen, J.; Ye, W.; Zhou, S.; Liu, H.; Wang, M. S. In situ atomic-scale observation of reversible potassium storage in Sb2S3@ carbon nanowire anodes. *Adv. Funct. Mater.* **2020**, *30* (52), No. 2005417.
(33) Wang, C.; Lu, J.; Tong, H.; Wu, S.; Wang, D.; Liu, B.; Cheng, L.; Lin, Z.; Hu, L.; Wang, H. Structural engineering of sulfur-doped carbon encapsulated bismuth sulfide core-shell structure for enhanced potassium storage performance. *Nano Res.* **2021**, *14* (10), 3545−3551.
(34) Cheng, H. F.; Zhou, Y.; Frost, R. L. Structure comparison of Orpiment and Realgar by Raman spectroscopy. *Spectrosc. Lett.* **2017**, *50* (1), 23−29.
(35) Carroll, E.; Buckley, D.; Mogili, N. V. V.; McNulty, D.; Sergio Moreno, M.; Glynn, C.; Collins, G.; Holmes, J. D.; Razeeb, K. M.; O'Dwyer, C. 2D Nanosheet Paint from Solvent-Exfoliated Bi2Te3 Ink. *Chem. Mater.* **2017**, *29* (17), 7390−7400.
(36) Hindmarsh, J. T.; McCurdy, R. F.; Savory, J. Clinical and environmental aspects of arsenic toxicity. *Crit. Rev. Clin. Lab. Sci.* **1986**, *23* (4), 315−347.
(37) Kapp, R. W. Arsenic: Toxicology and Health Effects. In *Encyclopedia of Food and Health*, Caballero, B.; Finglas, P. M.; Toldrá, F. Eds.; Academic Press, 2016; pp 256−265.
(38) Lim, Y. R.; Shojaei, F.; Park, K.; Jung, C. S.; Park, J.; Cho, W. I.; Kang, H. S. Arsenic for high-capacity lithium- and sodium-ion batteries. *Nanoscale* **2018**, *10* (15), 7047−7057.
(39) Luxa, J.; Bouša, D.; Zoller, F.; Fattakhova-Rohlfing, D.; Sofer, Z. Black phosphorus−arsenic alloys for lithium ion batteries. *FlatChem.* **2020**, *19*, No. 100143.
(40) Morimoto, N. The crystal structure of orpiment (As2S3) refined. *Mineral. J.* **1954**, *1* (3), 160−169.
(41) ŠiŠkins, M.; Lee, M.; Alijani, F.; Van Blankenstein, M. R.; Davidovikj, D.; Van Der Zant, H. S. J.; Steeneken, P. G. Highly anisotropic mechanical and optical properties of 2D layered As2S3 membranes. *ACS Nano* **2019**, *13* (9), 10845−10851.
(42) Debbichi, L.; Kim, H.; Björkman, T.; Eriksson, O.; Lebègue, S. First-principles investigation of two-dimensional trichalcogenide and sesquichalcogenide monolayers. *Phys. Rev. B* **2016**, *93* (24), No. 245307.
(43) Frost, R. L.; Martens, W. N.; Kloprogge, J. T. Raman spectroscopic study of cinnabar (HgS), realgar (As4S4), and orpiment (As2S3) at 298 and 77K. *Neues Jahrbuch für Mineralogie-Monatshefte* **2002**, *2002*, 469−480.
(44) Mamedov, S.; Drichko, N. Characterization of 2D As2S3 crystal by Raman spectroscopy. *AMRS Adv.* **2018**, *3* (6−7), 385−390.
(45) Razzetti, C.; Lottici, P. P. Polarization analysis of the Raman spectrum of As2S3 crystals. *Solid State Commun.* **1979**, *29* (4), 361−364.
(46) Backes, C.; Paton, K. R.; Hanlon, D.; Yuan, S.; Katsnelson, M. I.; Houston, J.; Smith, R. J.; McCloskey, D.; Donegan, J. F.; Coleman, J. N. Spectroscopic metrics allow in situ measurement of mean size and thickness of liquid-exfoliated few-layer graphene nanosheets. *Nanoscale* **2016**, *8* (7), 4311−4323.
(47) Hernandez, Y.; Nicolosi, V.; Lotya, M.; Blighe, F. M.; Sun, Z.; De, S.; McGovern, I. T.; Holland, B.; Byrne, M.; Gun'Ko, Y. K. High-yield production of graphene by liquid-phase exfoliation of graphite. *Nature Nanotechnol.* **2008**, *3* (9), 563−568.
(48) Harvey, A.; Backes, C.; Boland, J. B.; He, X.; Griffin, A.; Szydlowska, B.; Gabbett, C.; Donegan, J. F.; Coleman, J. N. Non-resonant light scattering in dispersions of 2D nanosheets. *Nat. Commun.* **2018**, *9* (1), 4553.
(49) Griffin, A.; Harvey, A.; Cunningham, B.; Scullion, D.; Tian, T.; Shih, C.-J.; Gruening, M.; Donegan, J. F.; Santos, E. J. G.; Backes, C. Spectroscopic size and thickness metrics for liquid-exfoliated h-BN. *Chem. Mater.* **2018**, *30* (6), 1998−2005.
(50) Holder, C. F.; Schaak, R. E. Tutorial on powder X-ray diffraction for characterizing nanoscale materials. *ACS Nano* **2019**, *13*, 7359−7365.
(51) Liu, K.; Dai, L.; Li, H.; Hu, H.; Yang, L.; Pu, C.; Hong, M.; Liu, P. Phase transition and metallization of orpiment by Raman spectroscopy, electrical conductivity and theoretical calculation under high pressure. *Materials* **2019**, *12* (5), 784.
(52) Zaumseil, P. High-resolution characterization of the forbidden Si 200 and Si 222 reflections. *J. Appl. Crystallogr.* **2015**, *48* (2), 528−532.
(53) Backes, C.; Campi, D.; Szydlowska, B. M.; Synnatschke, K.; Ojala, E.; Rashvand, F.; Harvey, A.; Griffin, A.; Sofer, Z.; Marzari, N. Equipartition of energy defines the size−thickness relationship in liquid-exfoliated nanosheets. *ACS Nano* **2019**, *13* (6), 7050−7061.
(54) Coleman, J. N. *Are Nanotube Networks the Key to High-Rate, High Capacity Lithium Ion Batteries?*; The Electrochemical Society, Inc., 2020; p 589
(55) Park, S.-H.; King, P. J.; Tian, R.; Boland, C. S.; Coelho, J.; Zhang, C.; McBean, P.; McEvoy, N.; Kremer, M. P.; Daly, D. High areal capacity battery electrodes enabled by segregated nanotube networks. *Nature Energy* **2019**, *4* (7), 560−567.
(56) Gabbett, C.; Doolan, L.; Synnatschke, K.; Gambini, L.; Coleman, E.; Kelly, A. G.; Liu, S.; Caffrey, E.; Munuera, J.; Murphy, C.; et al. Morphological Characterisation of Printed Nanostructured Networks using High-resolution 3D FIB-SEM Nanotomography. *Nature Commun.* 2023. (in press)
(57) Wang, J.; Fan, L.; Liu, Z.; Chen, S.; Zhang, Q.; Wang, L.; Yang, H.; Yu, X.; Lu, B. In situ alloying strategy for exceptional potassium ion batteries. *ACS Nano* **2019**, *13* (3), 3703−3713.
(58) Nithya, C.; Modigunta, J. K. R.; In, I.; Kim, S.; Gopukumar, S. Bi2S3 Nanorods Deposited on Reduced Graphene Oxide for Potassium-Ion Batteries. *ACS Appl. Nano Mater.* **2023**, *6* (7), 6121−6132.
(59) Liu, Y.; Tai, Z.; Zhang, J.; Pang, W. K.; Zhang, Q.; Feng, H.; Konstantinov, K.; Guo, Z.; Liu, H. K. Boosting potassium-ion batteries by few-layered composite anodes prepared via solution-triggered one-step shear exfoliation. *Nat. Commun.* **2018**, *9* (1), 3645.
(60) Zhou, J.; Wang, L.; Yang, M.; Wu, J.; Chen, F.; Huang, W.; Han, N.; Ye, H.; Zhao, F.; Li, Y. Hierarchical VS2 nanosheet assemblies: a universal host material for the reversible storage of alkali metal ions. *Adv. Mater.* **2017**, *29* (35), No. 1702061.
(61) Gu, S.; Xiao, N.; Wu, F.; Bai, Y.; Wu, C.; Wu, Y. Chemical synthesis of K2S2 and K2S3 for probing electrochemical mechanisms in K−S batteries. *ACS Energy Lett.* **2018**, *3* (12), 2858−2864.
(62) Du, Y.; Zhang, Z.; Xu, Y.; Bao, J.; Zhou, X. Metal sulfide-based potassium-ion battery anodes: storage mechanisms and synthesis strategies. *Acta Phys.-Chim. Sin.* **2022**, *38*, No. 2205017.
(63) Cao, L.; Luo, B.; Xu, B.; Zhang, J.; Wang, C.; Xiao, Z.; Li, S.; Li, Y.; Zhang, B.; Zou, G. Stabilizing intermediate phases via efficient

https://doi.org/10.1021/acsnano.4c03501
ACS Nano 2024, 18, 20213−20225

entrapment effects of layered VS4/SnS@ C heterostructure for ultralong lifespan potassium-ion batteries. *Adv. Funct. Mater.* **2021**, *31* (36), No. 2103802.
(64) Shpotyuk, O.; Demchenko, P.; Shpotyuk, Y.; Bujňáková, Z.; Baláž, P. Medium-range structural changes in glassy As2S3 driven by high-energy mechanical milling. *J. Non-Cryst. Solids* **2019**, *505*, 347−353.
(65) Konkena, B.; Kaur, H.; Tian, R.; Gabbett, C.; McCrystall, M.; Horvath, D. V.; Synnatschke, K.; Roy, A.; Smith, R.; Nicolosi, V. Liquid Processing of Interfacially Grown Iron-Oxide Flowers into 2D-Platelets Yields Lithium-Ion Battery Anodes with Capacities of Twice the Theoretical Value. *Small* **2022**, *18* (39), No. 2203918.
(66) Fan, H.-N.; Wang, X.-Y.; Yu, H.-B.; Gu, Q.-F.; Chen, S.-L.; Liu, Z.; Chen, X.-H.; Luo, W.-B.; Liu, H.-K. Enhanced Potassium Ion Battery by Inducing Interlayer Anionic Ligands in MoS1.5Se0.5 Nanosheets with Exploration of the Mechanism. *Adv. Energy Mater.* **2020**, *10* (21), No. 1904162.
(67) Ma, X.; Fu, H.; Shen, J.; Zhang, D.; Zhou, J.; Tong, C.; Rao, A. M.; Zhou, J.; Fan, L.; Lu, B. Green Ether Electrolytes for Sustainable High-voltage Potassium Ion Batteries. *Angew. Chem., Int. Ed.* **2023**, *62* (49), No. e202312973.
(68) Geng, Y.; Fu, H.; Hu, Y.; Rao, A. M.; Fan, L.; Zhou, J.; Lu, B. Molecular-level design for a phosphate-based electrolyte for stable potassium-ion batteries. *Appl. Phys. Lett.* **2024**, *124* (6), No. 063901.
(69) Fan, L.; Xie, H.; Hu, Y.; Caixiang, Z.; Rao, A. M.; Zhou, J.; Lu, B. A tailored electrolyte for safe and durable potassium ion batteries. *Energy Environ. Sci.* **2023**, *16* (1), 305−315.
(70) Horvath, D. V.; Coelho, J.; Tian, R.; Nicolosi, V.; Coleman, J. N. Quantifying the Dependence of Battery Rate Performance on Electrode Thickness. *ACS Appl. Energy Mater.* **2020**, *3* (10), 10154−10163.
(71) Tian, R.; Alcala, N.; O'Neill, S. J. K.; Horvath, D. V.; Coelho, J.; Griffin, A. J.; Zhang, Y.; Nicolosi, V.; O'Dwyer, C.; Coleman, J. N. Quantifying the Effect of Electronic Conductivity on the Rate Performance of Nanocomposite Battery Electrodes. *ACS Appl. Energy Mater.* **2020**, *3* (3), 2966−2974.
(72) Tian, R.; Breshears, M.; Horvath, D. V.; Coleman, J. N. The Rate Performance of Two-Dimensional Material-Based Battery Electrodes May Not Be as Good as Commonly Believed. *ACS Nano* **2020**, *14* (3), 3129−3140.
(73) Tian, R.; Park, S.-H.; King, P. J.; Cunningham, G.; Coelho, J.; Nicolosi, V.; Coleman, J. N. Quantifying the factors limiting rate performance in battery electrodes. *Nat. Commun.* **2019**, *10* (1), 1933.
(74) Horvath, D. V.; Tian, R.; Gabbett, C.; Nicolosi, V.; Coleman, J. N. Quantifying the Effect of Separator Thickness on Rate Performance in Lithium-Ion Batteries. *J. Electrochem. Soc.* **2022**, *169* (3), No. 030503.
(75) Park, S.-H.; Tian, R.; Coelho, J.; Nicolosi, V.; Coleman, J. N. Quantifying the Trade-Off between Absolute Capacity and Rate Performance in Battery Electrodes. *Adv. Energy Mater.* **2019**, *9* (33), No. 1901359.
(76) Coleman, J. N.; Tian, R. Developing models to fit capacity-rate data in battery systems. *Curr. Opin. Electrochem.* **2020**, *21*, 1−6.
(77) Tian, R.; Griffin, A.; McCrystall, M.; Breshears, M.; Harvey, A.; Gabbett, C.; Horváth, D. V.; Backes, C.; Jing, Y.; Heine, T.; et al. Liquid Exfoliated SnP3 Nanosheets for Very High Areal Capacity Lithium-Ion Batteries. *Adv. Energy Mater.* **2021**, *11* (4), No. 2002364.
(78) Konkena, B.; Kaur, H.; Tian, R.; Gabbett, C.; McCrystall, M.; Horvath, D. V.; Synnatschke, K.; Roy, A.; Smith, R.; Nicolosi, V.; et al. Liquid Processing of Interfacially Grown Iron-Oxide Flowers into 2D-Platelets Yields Lithium-Ion Battery Anodes with Capacities of Twice the Theoretical Value. *Small* **2022**, *18* (39), No. 2203918.
(79) Kaur, H.; Konkena, B.; Gabbett, C.; Smith, R.; McCrystall, M.; Tian, R.; Roy, A.; Carey, T.; Vega-Mayoral, V.; Nicolosi, V.; et al. Amorphous 2D-Nanoplatelets of Red Phosphorus Obtained by Liquid-Phase Exfoliation Yield High Areal Capacity Na-Ion Battery Anodes. *Adv. Energy Mater.* **2023**, *13* (6), No. 2203013.
(80) Kaur, H.; Tian, R.; Roy, A.; McCrystall, M.; Horvath, D. V.; Lozano Onrubia, G.; Smith, R.; Ruether, M.; Griffin, A.; Backes, C. Production of Quasi-2D Platelets of Nonlayered Iron Pyrite (FeS2) by Liquid-Phase Exfoliation for High Performance Battery Electrodes. *ACS Nano* **2020**, *14* (10), 13418−13432.
(81) Chen, T.; Kaur, H.; McCrystall, M.; Tian, R.; Roy, A.; Smith, R.; Horvath, D. V.; Maughan, J.; Konkena, B.; Venkatesan, M. Liquid phase exfoliation of nonlayered non-van der Waals iron trifluoride (FeF3) into 2D-platelets for high-capacity lithium storing cathodes. *FlatChem.* **2022**, *33*, No. 100360.

https://doi.org/10.1021/acsnano.4c03501
ACS Nano 2024, 18, 20213−20225